Article

Single-Fiber Reflectance Spectroscopy of Isotropic-Scattering Medium: An Analytic Perspective to the Ratio-of-Remission in Steady-State Measurements

Daqing Piao [1],* and Joel W. Slaton [2]

[1] School of Electrical and Computer Engineering, Oklahoma State University, Stillwater, OK 74078, USA

[2] Department of Urology, University of Oklahoma Health Sciences Center, Oklahoma, OK 73104, USA; E-Mail: joel-slaton@ouhsc.edu

* Author to whom correspondence should be addressed; E-Mail: daqing.piao@okstate.edu.

Abstract: Recent focused Monte Carlo and experimental studies on steady-state single-fiber reflectance spectroscopy (SfRS) from a biologically relevant scattering medium have revealed that, as the dimensionless reduced scattering of the medium increases, the SfRS intensity increases monotonically until reaching a plateau. The SfRS signal is semi-empirically decomposed to the product of three contributing factors, including a ratio-of-remission (RoR) term that refers to the ratio of photons remitting from the medium and crossing the fiber-medium interface over the total number of photons launched into the medium. The RoR is expressed with respect to the dimensionless reduced scattering parameter $\mu_s' d_{fib}$, where μ_s' is the reduced scattering coefficient of the medium and d_{fib} is the diameter of the probing fiber. We develop in this work, under the assumption of an isotropic-scattering medium, a method of analytical treatment that will indicate the pattern of RoR as a function of the dimensionless reduced scattering of the medium. The RoR is derived in four cases, corresponding to in-medium (applied to interstitial probing of biological tissue) or surface-based (applied to contact-probing of biological tissue) SfRS measurements using straight-polished or angle-polished fiber. The analytically arrived surface-probing RoR corresponding to single-fiber probing using a $15°$ angle-polished fiber over the range of $\mu_s' d_{fib} = \left(10^{-2}\ 10^{3}\right)$ agrees with previously reported similarly configured experimental measurement from a scattering medium that has a Henyey–Greenstein scattering phase function with an anisotropy factor of 0.8. In cases of a medium scattering light

anisotropically, we propose how the treatment may be furthered to account for the scattering anisotropy using the result of a study of light scattering close to the point-of-entry by Vitkin *et al.* (*Nat. Commun.* **2011**, doi:10.1038/ncomms1599).

Keywords: light propagation in tissues; single-fiber reflectance spectroscopy; photon migration; functional monitoring and imaging

1. Introduction

Reflectance spectroscopy [1,2] is simple to setup, and the machinery is relatively low cost. Reflectance spectroscopy instrumented by using single-fiber probe, which is generally referred to as single-fiber reflectance spectroscopy (SfRS) [3–6], delivers light to a turbid medium and detects the light returning to the collection aperture of the same fiber after the photons have experienced some scattering/attenuation events in the medium. The use of fiber-optic probes of small tip profiles has allowed measurement of biological tissue through the lumen of small needles for interstitial or percutaneous probing to assist fine-needle aspiration procedures [7,8] and laser-based treatment protocols [9,10]. Fiber-probing that can be administered through the instrument channels of endoscopes has also shown the promise of assessing the deterioration of microvasculature in superficial tissue, like the wall of bladder [11].

The setup of SfRS (or reflectance spectroscopy using a small tip-profile) being simple, the return of spectroscopic information renders the evaluation of absorbing [5–8] or fluorescing [12–15] chromophores, assessment of changes in tissue scattering [9,10] and further analysis of sizing information of the scattering particles [16,17] within the interrogated medium. To quantitate the measurement by SfRS as the endpoint is to estimate tissue optical properties based on the measurements, it is imperative to have a working model of the dependence of SfRS signal intensity (which is spectrally resolved) upon tissue optical properties (also spectrally resolved). Such a model process also facilitates cross-system validations by the ability to reproduce or cross-exam absolute signals for the same set of measurands (tissue optical properties) across different SfRS systems. Some earlier studies have examined the fiber-optical aspect of the SfRS signal, necessitating removing the internal specular reflections from the collected signal [18] and accounting for the collection efficiency of a single fiber [19] as being limited by the numerical aperture. The relationship between SfRS intensity and optical properties was initially studied by Moffit and Prahl [3]; that yielded qualitative estimates of the dependence of the SfRS signal upon the optical properties of the medium. Recently, a series of studies, based on extensive Monte Carlo (MC) simulations and experimental validations, have quantitated the effect of optical properties on SfRS measurement [20–26]. Among these studies, Kanick *et al*. investigated the dependence of the effective photon path length, as well as sampling depth [20,21] on the optical properties of the sampled medium. Kanick *et al*. and Gamm *et al*. further studied the relationship between SfRS signal intensity and the scattering properties of the medium [22,23]. As is expected, the scattering phase function [27–29] influences the SfRS signal intensity [22–26], because the photons to be collected by the single-fiber probe are scattered at or near the point-of-entry; but when the effect of the phase function is lumped into the reduced scattering coefficient μ'_s, the SfRS is

accurately quantitated with respect to a dimensionless reduced scattering term $\mu_s' d_{fib}$, where d_{fib} is the diameter of the probing fiber. Specifically, the MC and experimental measurements have confirmed that steady-state SfRS intensity increases monotonically *versus* $\mu_s' d_{fib}$ until approximately $\mu_s' d_{fib} > 10$, when approaching an asymptotic limit [22,23]. The dependence of steady-state SfRS intensity upon the reduced scattering coefficient μ_s' and absorption coefficient μ_a has been formulated [22–26] to a set of semi-empirical equations:

$$R_{SfRS}(\mu_a, \mu_s') = R_{remission}(\mu_s')\eta_{collection}(\mu_s')\exp\left[-\mu_a\left\langle L(\mu_a, \mu_s')\right\rangle\right] \tag{1}$$

$$R_{remission}(\mu_s') = \left[\frac{\left(\mu_s' d_{fib}\right)^{p_2}}{p_1 + \left(\mu_s' d_{fib}\right)^{p_2}}\right] \tag{2}$$

$$\eta_{collection}(\mu_s') = \eta_{\lim}\left[1 + p_3\exp\left(-p_1\mu_s' d_{fib}\right)\right] \tag{3}$$

$$\left\langle L(\mu_a, \mu_s')\right\rangle = \frac{p_4 d_{fib}}{\left(\mu_s' d_{fib}\right)^{p_5}\left[p_6 + \left(\mu_a d_{fib}\right)^{p_6}\right]} \tag{4}$$

where p_1 to p_6 are fitted constants, some having a dependence on the scattering phase function of the medium, and $\eta_{\lim}$ is determined by the acceptance angle of the fiber and the refractive index of the medium. This set of equations essentially decomposes the SfRS signal into the product of three contributing factors: (1) a reduced scattering-dependent term $R_{remission}(\mu_s')$ that accounts for the ratio of photons remitting from the medium and crossing the area of the fiber facet over the total number of photons launched into the medium, which will be referred to as the "ratio-of-remission" and abbreviated as RoR in this work; (2) a reduced scattering-dependent term $\eta_{collection}(\mu_s')$ that represents the collection efficiency of the fiber due to the limited numerical aperture; and (3) an absorption-dependent term $\exp\left[-\mu_a\left\langle L(\mu_a, \mu_s')\right\rangle\right]$ that is responsible for the attenuation of photons in the medium due exclusively to absorption and that is modeled using the modified Beer–Lambert law over an effective path length of $\left\langle L(\mu_a, \mu_s')\right\rangle$, which is, however, mainly determined by the reduced scattering of the medium.

It is noted that the dimensionless reduced scattering term $\mu_s' d_{fib}$ appearing in the set of Equations (1)–(4) is a measure of the relative scale of the size of the probing fiber with respect to the transport scattering path length of the light in the medium. Intuitively, therefore, the bigger the fiber with respect to the transport scattering path length of the medium, the more scattered light the fiber will collect. The increased collection of the scattered light by the fiber will, however, approach a limit, when the scattering of the medium reaches the condition that the backscattering event occurs at positions very close to the fiber facet, making only the portion of the scattered light that is within the numerical aperture of the fiber collectable. Apparently, an increase of the absorption coefficient μ_a of the medium will reduce the light collected by the single-fiber probe. In establishing the set of semi-empirical Equations (1)–(4), the effect of the numerical aperture of the fiber on the collection of the scattering photons is taken care of by the $\eta_{collection}(\mu_s')$ term, leaving the $R_{remission}(\mu_s')$ term to exclusively account for the relative scale of the fiber diameter with respect to the reduced scattering path length. The empirical formula for $R_{remission}(\mu_s')$ has proven accurate and convenient for characterizing SfRS signal intensity in a variety of applications [7,8,24–26], with the need to only adjust the a few constants according to the scattering phase function, if known. Given that $R_{remission}(\mu_s')$, shown in Equation (2), is formulated empirically, other forms of $R_{remission}(\mu_s')$ that are quantitatively very

close to the one shown in Equation (2) shall not be excluded in evaluating Equation (1). A more fundamental plausibility pertinent to $R_{remission}(\mu_s')$ is whether the $R_{remission}(\mu_s')$ term can be developed analytically, not empirically.

An accurate analytical model of how the tissue optical properties affect $R_{remission}(\mu_s')$ shall originate from the radiative transfer equation [29,30] that employs the scattering coefficient μ_s and takes into account the anisotropy g of the scattering [31–37]. The successful use of the reduced scattering coefficient $\mu_s' = \mu_s(1-g)$ in the semi-empirical modeling of the RoR term $R_{remission}(\mu_s')$, however, suggests that the global pattern of $R_{remission}(\mu_s')$ may be reached analytically by direct utilization of μ_s'. When many events of anisotropic scattering happening at a shorter scattering path length of $1/\mu_s$ contribute to the detected photon fluence, the combined effect could be equalized to a lesser number of isotropic scattering events happening at a much longer path length of $1/\mu_s'$, as is the underlining motivation for introducing μ_s' into describing the light propagation in the presence of scattering

This work aims at developing an analytical pathway that may arrive at the quantitative pattern (but not necessarily the exact formulae) of the RoR that is displayed by Equation (2). The derivation will be illustrated in four cases, corresponding to in-medium or surface-based SfRS measurements by using straight-polished or angle-polished fiber. The angle-polished fiber is frequently used in experimental SfRS as a result of the need to abate excessive specular reflection from the fiber-tissue interface that impairs measurement from the medium of interest. The analysis shown in this work provides insight to the difference of SfRS intensities between two different geometries of probing the tissue, probing interstitially and probing by surface-contact of the medium. The effect of the geometry of probing the tissue-medium by the single fiber probe, *i.e.*, interstitial or contact-based, on SfRS intensity has to the authors' knowledge not been attended previously. It is demonstrated that the analytically computed SfRS corresponding to a $15°$ angle-polished fiber in a semi-infinite medium geometry over the range of $\mu_s'd_{fib} = \left(10^{-2}\ 10^3\right)$ agrees with the previously reported experimental results performed in a surface-probing configuration, for a medium that presented a Henyey–Greenstein (HG) scattering phase function with an anisotropy factor of 0.8. In cases of medium scattering light anisotropically, we will discuss how the analytical treatment may be furthered to account for the scattering anisotropy.

2. Analytic Development

An ideal light source for SfRS has a uniform intensity profile across the broad spectrum of interest, as is schematically illustrated in Figure 1. With such a light source, what is measured out of the single probing fiber represents exclusively the spectrally-resolved tissue reflectivity $R_{SfRS}(\lambda)$ that was formulated semi-empirically in Equation (1). To derive the $R_{remission}(\lambda)$ of $R_{SfRS}(\lambda)$, we refer to the inset in Figure 1 for a hypothetical examination of the path of a single photon in the medium between leaving the fiber and reaching the fiber after experiencing scattering events. By treating the light launched by the fiber to the tissue as originating from a spatially impulsive source, using the same fiber to deliver light to tissue and to collect light from tissue can be assimilated to either of the following two configurations, as long as the collection of one photon is concerned: (1) a dual-fiber configuration with a photon of interest being launched by a delivery fiber then collected by another fiber and letting the distance between the delivery and collection fibers approaching the size of the single-fiber probe; and (2) a single-fiber dual-point configuration, wherein the photon of interest is

launched into the medium at the center point of the fiber facet, then collected by the same fiber at an off-center point of the fiber facet, as revealed by the hypothetical "magnified" view of the inset. Although either of these two approximations could possibly facilitate analysis of $R_{remmission}(\lambda)$, the second one hypothesizing single-fiber dual-points will be shown in this work in expressing $R_{remmission}(\lambda)$ as a function of μ'_s and the fiber dimensional parameters (fiber diameter and polishing angle of the fiber tip). The analytical evaluation will be conducted in an infinite geometry and a semi-infinite geometry of the medium. Distinguishing between the two geometries is necessary, because when the fiber probe is placed in contact with the surface of the medium, as in cases of MC or the associated experiments [21–23], the tissue to the photon propagation is a half-space with a planar boundary that essentially conforms to a semi-infinite medium geometry. When the fiber probe is inserted into the medium, such as in cases for fine-needle aspiration procedures [7,8] or laser-based treatment protocols [9,10], the tissue to the photon propagation is more suitable to be described by an infinite-medium geometry than a half-space or semi-infinite geometry. Note that the effect of the limited numerical aperture of the fiber to the collection of photon flux has been separately accounted for in $R_{SfRS}(\lambda)$ by $\eta_{collection}$. Consequently the $R_{remission}(\mu'_s)$ term stands for the ratio of photons remitting from the medium and crossing the area of the fiber facet over the total number of photons launched into the medium, but not the ratio of photons collected by the fiber over the total number of photons launched into the medium, as the latter has to involve the numerical aperture, which is addressed by $\eta_{collection}$. The different refractive indices of the fiber and the tissue across the tissue-fiber interface, however, will cause part of the photon flux at the fiber-tissue interface to be bounced back to the tissue; the amount of photons returning to the tissue is readily modeled by Fresnel reflection as is shown in the following derivations of $R_{remission}(\mu'_s)$.

We consider the tissue to be modeled for steady-state RoR to have the following homogeneous and wavelength-dependent optical properties (for convenience, these properties are presented without the argument of wavelength λ in their respective symbols): absorption coefficient μ_a, reduced scattering coefficient μ'_s, diffusion coefficient $D = 1/(3\mu'_s)$ and effective attenuation coefficient $\mu_{eff} = \sqrt{\mu_a/D}$.

Figure 1. An ideal light source for single-fiber reflectance spectroscopy (SfRS) has a uniform intensity profile across the broad spectrum of interest. With such a light source, what is measured out of the light collected from the single probing fiber represents exclusively the tissue reflectivity as a function of wavelength, with which the optical properties, including absorption and reduced scattering coefficients of localized bulk tissue, may be recovered. The inset enclosed by the dashed circle indicates that the single-fiber configuration can be approximated by a dual-fiber configuration in its limites case or a dual-path configuration: (1) a dual-fiber configuration with separate delivery and collection fibers, by letting the distance between the delivery and collection fibers approaching the size of the fiber; (2) a single-fiber dual-point configuration, wherein the points of light delivery and light collection are different, but both are located at the facet of the fiber tip. Either of these two treatments would facilitate analytical evaluation with the assumption of photon-diffusion principles.
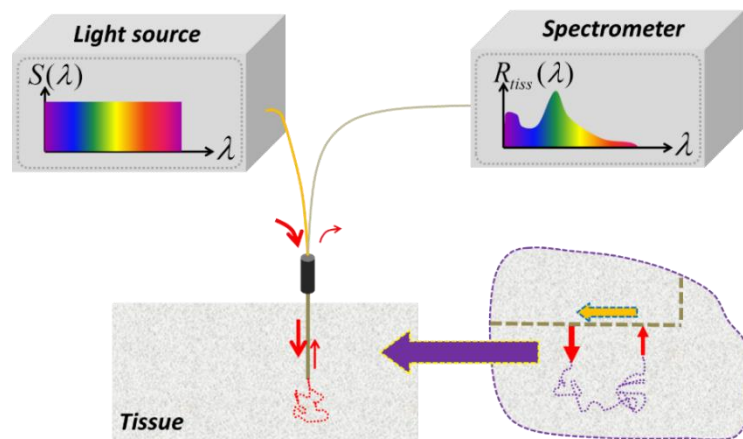

2.1. Ratio-of-Remission Associated with Steady-State Probing in an Infinite Tissue Geometry Using a Straight-Polished Fiber

The single-fiber dual-point configuration to represent SfRS by using a straight-polished fiber embedded in the tissue is schematically illustrated in Figure 2A. The associated path of a single photon trajectory is hypothesized in Figure 2B. Under cylindrical coordinates of $\vec{r}(\rho, \varphi, z)$, the following symbols and notations are introduced:

- The center of the fiber facet is located at $\vec{r}_c(0,0,0)$. A point at the fiber facet is $\vec{r}_d(\rho, \varphi, 0)$, at which the position-specific photon fluence rate and flux are evaluated.
- The light that is initially directionally-launched into the medium along the direction of the fiber axis is represented by an equivalent isotropic point source, with the same intensity of the incident light, that is located at $\vec{r}_{real}(0,0,z_a)$, where $z_a = 1/\mu'_s$ [38]. Note that the positive direction of the z-axis points away from the fiber or downward hereinafter through Figures 3–5.
- The distance between the equivalent isotropic point source $\vec{r}_{real}$ and the detector point $\vec{r}_d(\rho, \varphi, 0)$ is $l_{real} = |\vec{r}_{real} - \vec{r}_d| = \sqrt{\rho^2 + z_a^2}$. The acute angle formed by the line of l_{real} with respect to the axis of the fiber is $\theta_{real} = \tan^{-1}(\rho/z_a)$.

- The radius of the fiber is denoted as r_{fib}, or $r_{rib} = d_{fib}/2$, for convenience.

- The refractive indices of the fiber and tissue are n_{fib} and n_{tiss}, respectively. Generally $n_{fib} > n_{tiss}$.

Figure 2. (**A**) Schematic of an idealized geometry for placing a fiber with a diameter of d_{fib} and a straight-polished tip within a turbid medium. The same fiber is used for launching light into and collecting light from the medium. A dual-point configuration approximates the light leaving and returning to the fiber. (**B**) The light that is initially directionally-launched into the medium is represented by an equivalent isotropic source that is located at $\vec{r}_{real}(0,0,z_a)$, where $z_a = 1/\mu_s'$. The distance between the equivalent source $\vec{r}_{real}$ and a detector point $\vec{r}_d(\rho,\varphi,0)$ is l_{real}. The acute angle formed by the line of l_{real} with respect to the axis of the fiber is θ_{real}.
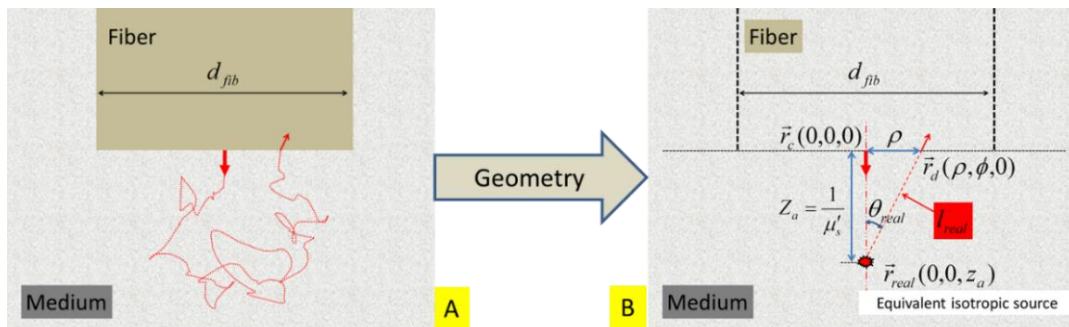
For a light of unit intensity that is launched into the medium at the center of the fiber facet, the photon fluence rate evaluated at $\vec{r}_d(\rho,\varphi,0)$ as a result of the equivalent isotropic point source of unity intensity at $\vec{r}_{real}(0,0,z_a)$ is:

$$\Psi_{\inf}(\vec{r}_d) = \frac{1}{4\pi D}\frac{\exp(-\mu_{eff}l_{real})}{l_{real}} \tag{5}$$

The photon flux evaluated at $\vec{r}_d(\rho,\varphi,0)$ is proportional to the spatial gradient of the photon fluence rate as the following:

$$\vec{J}_{\inf}(\vec{r}_d) = -D\cdot\nabla\Psi_{\inf}(\vec{r}_d) = -\frac{1}{4\pi}\cdot\frac{\partial}{\partial l_{real}}\left(\frac{\exp(-\mu_{eff}l_{real})}{l_{real}}\right)\hat{l}_{real} = \frac{1}{4\pi}\cdot\frac{\exp(-\mu_{eff}l_{real})}{(l_{real})^2}\left(\mu_{eff}l_{real}+1\right)\hat{l}_{real} \tag{6}$$

where $\hat{l}_{real}$ is the unit vector pointing from $\vec{r}_{real}$ to $\vec{r}_d$. The components of the photon flux that are parallel to the fiber facet will not contribute to the signal collected by the fiber, and only the axial component along the $-\hat{z}$ direction will have the chance to cross the fiber facet. The photon flux at the medium side and reaching the fiber facet at point $\vec{r}_d(\rho,\varphi,0)$ in a direction normal to the fiber facet is:

$$\vec{J}^{\,z}_{\inf}(\vec{r}_d) = \left|\vec{J}_{\inf}(\vec{r}_d)\right|\cos\theta_{fib}(-\hat{z}) = \frac{1}{4\pi}\cdot\frac{\exp(-\mu_{eff}\,l_{real})}{(l_{real})^2}\left(\mu_{eff}\,l_{real}+1\right)\cos\theta_{real}(-\hat{z})$$

$$= \frac{1}{4\pi}\cdot\frac{z_a}{(l_{real})^3}\left(\mu_{eff}\,l_{real}+1\right)\exp(-\mu_{eff}\,l_{real})(-\hat{z}) \tag{7}$$

The ratio of this normal component of photon flux that is transmitted across the fiber facet will be determined by the Fresnel formula of $T_{norm}=1-R_{norm}$, where $R_{norm}=\left[\left(n_{tiss}-n_{fib}\right)/\left(n_{tiss}+n_{fib}\right)\right]^2$. The resulting photon flux at point $\vec{r}_d(\rho,\varphi,0)$ that is normal to and crosses the fiber facet is:

$$\vec{J}^{\,fib}_{\inf}(\vec{r}_d) = \frac{1}{4\pi}T_{norm}\cdot\frac{z_a}{(l_{real})^3}\left(\mu_{eff}\,l_{real}+1\right)\exp(-\mu_{eff}\,l_{real})(-\hat{z}) \tag{8}$$

The total remission over the dimension of the fiber is then obtained by integrating $\vec{J}^{\,fib}_{\inf}(\vec{r}_d)$ over the total area of the fiber facet as:

$$R^{\inf}_{remission}(\mu'_s) = \int_0^{2\pi}d\phi\int_0^{r_{fib}}\left|\vec{J}^{\,fib}_{\inf}(\vec{r}_d)\right|\rho\cdot d\rho$$

$$= \frac{1}{4\pi}T_{norm}\cdot\int_0^{2\pi}d\phi\int_0^{r_{fib}}\frac{z_a}{(l_{real})^2}\left(\mu_{eff}\,l_{real}+1\right)\exp(-\mu_{eff}\,l_{real})\rho\cdot d\rho \tag{9}$$

Note that $\rho^2 = l_{real}^2 - z_a^2$, then $\rho\cdot d\rho = l_{real}\cdot dl_{real}$, so Equation (9) changes to:

$$R^{\inf}_{remission}(\mu'_s) = \frac{1}{4\pi}T_{norm}\cdot(2\pi)\int_{z_a}^{\sqrt{r_{fib}^2+z_a^2}}\frac{z_a}{(l_{real})^2}\left(\mu_{eff}\,l_{real}+1\right)\exp(-\mu_{eff}\,l_{real})\cdot dl_{real}$$

$$= \frac{1}{2}T_{norm}\cdot\left(\exp(-\mu_{eff}\,z_a) - \frac{z_a}{\sqrt{r_{fib}^2+z_a^2}}\exp(-\mu_{eff}\sqrt{r_{fib}^2+z_a^2})\right) \tag{10}$$

By expanding the exponential functions in Equation (10) up to the first order term in their respective Taylor series, the absorption dependence is removed to give the following RoR that is associated with the use of a straight-polished fiber in an infinite domain of tissue medium:

$$R^{\inf}_{remission}(\mu'_s) = \frac{1}{2}(1-R_{norm})\cdot\left(1 - \frac{z_a}{\sqrt{r_{fib}^2+z_a^2}}\right) \tag{11}$$

2.2. Ratio-of-Remission Associated with Steady-State Probing in a Semi-Infinite Tissue Geometry Using a Straight-Polished Fiber

The single-fiber dual-point configuration to represent a straight-polished fiber in contact with the surface of a half-plane tissue is schematically illustrated in Figure 3A. The associated path of a single photon trajectory, now in a semi-infinite medium geometry, is hypothesized in Figure 3B. The symbols introduced in Section 2.1 are used here whenever applicable. Additional symbols/entities in association with the semi-infinite geometry are given in the following section:

Figure 3. (**A**) Schematic of an idealized geometry for placing a fiber with a diameter of d_{fib} and a straight-polished tip at the surface of a turbid medium. The same fiber is used for launching light into and collecting light from the medium. A dual-point configuration approximates the light leaving and returning to the fiber. (**B**) The light that is initially directionally-launched into the medium is represented by an equivalent isotropic source that is located at $\vec{r}_{real}(0,0,z_a)$. The distance between the equivalent source $\vec{r}_{real}$ and a detector point $\vec{r}_d(\rho,\varphi,0)$ is l_{real}, and the acute angle formed by the line of l_{real} with respect to the axis of the fiber is θ_{real}. An "extrapolated" boundary is located at z_b away from the physical boundary of the medium. The image of the source $\vec{r}_{real}$ with respect to the "extrapolated" boundary is located at $\vec{r}_{imag}(0,0,-(z_a+2z_b))$. The distance between the image source $\vec{r}_{imag}$ and the detector point $\vec{r}_d$ is l_{imag}. The acute angle formed by the line of l_{imag} w.r.t the axis of the fiber is θ_{imag}.
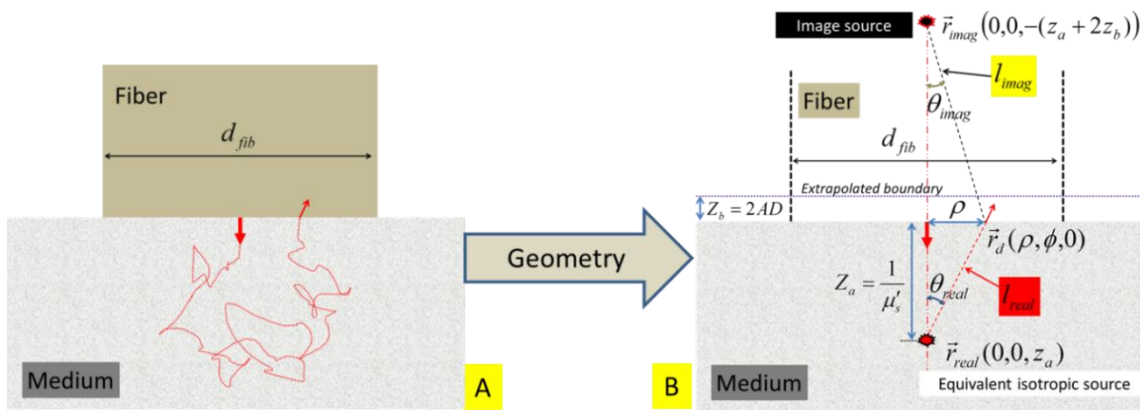
- The air-tissue interface is a semi-infinite planar boundary to the photon propagation. The boundary effect to the photon propagation in the medium can be accounted for by introducing an "extrapolated boundary" [38–41] on which the photon fluence rate is set zero.
- The "extrapolated boundary" is located at a distance of z_b from the air-tissue interface, with $z_b = 2AD$ $A = (1+\xi)/(1-\xi)$, $\xi = -1.440 n_{rel}^{-2} + 0.710 n_{rel}^{-1} + 0.668 + 0.0636 n_{rel}$ and $n_{rel} = n_{tiss}/n_{air}$, where n_{air} is the refractive index of the air.
- The equivalent isotropic point source is located at $\vec{r}_{real}(0,0,z_a)$. The image of the isotropic point source $\vec{r}_{real}$ with respect to the extrapolated boundary is located at $\vec{r}_{imag}(0,0,-(z_a+2z_b))$. The "image" source has the opposite intensity of the "real" source at $\vec{r}_{real}$.
- The distance between the "real" source $\vec{r}_{real}$ and the detector point $\vec{r}_d(\rho,\varphi,0)$ is $l_{real} = |\vec{r}_{real} - \vec{r}_d| = \sqrt{\rho^2 + z_a^2}$. The acute angle formed by the line of l_{real} with the axis of the fiber is $\theta_{real} = \tan^{-1}(\rho/z_a)$. The distance between the "image" source $\vec{r}_{imag}$ and $\vec{r}_d(\rho,\varphi,0)$ is $l_{imag} = |\vec{r}_{imag} - \vec{r}_d| = \sqrt{\rho^2 + (z_a+2z_b)^2}$. The acute angle formed by the line of l_{imag} with the axis of the fiber is $\theta_{imag} = \tan^{-1}[\rho/(z_a+2z_b)]$.

The steady-state photon fluence rate at $\vec{r}_d(\rho,\varphi,0)$ is:

$$\Psi_{semi}(\vec{r}_d) = \frac{1}{4\pi D} \cdot \left[\frac{\exp(-\mu_{eff} l_{real})}{l_{real}} - \frac{\exp(-\mu_{eff} l_{imag})}{l_{imag}} \right] \tag{12}$$

The photon flux at $\vec{r}_d(\rho, \varphi, 0)$ is:

$$\vec{J}_{semi}(\vec{r}_d) = -D \cdot \nabla \Psi_{semi}(\vec{r}_d) = \frac{1}{4\pi} \cdot \left[\frac{\exp(-\mu_{eff} l_{real})}{(l_{real})^2} (\mu_{eff} l_{real} + 1)\hat{r}_{real} - \frac{\exp(-\mu_{eff} l_{imag})}{(l_{imag})^2} (\mu_{eff} l_{imag} + 1)\hat{r}_{imag} \right] \tag{13}$$

As only the axial component of the photon flux along the $-\hat{z}$ direction will cross the fiber facet, the photon flux at the medium side and normal to the fiber facet at $\vec{r}_d(\rho, \varphi, 0)$ is:

$$\vec{J}_{semi}^{z}(\vec{r}_d) = \frac{1}{4\pi} \cdot \left[\frac{z_a}{(l_{real})^3}(\mu_{eff} l_{real} + 1)\exp(-\mu_{eff} l_{real}) + \frac{z_a + 2z_b}{(l_{imag})^3}(\mu_{eff} l_{imag} + 1)\exp(-\mu_{eff} l_{imag}) \right](-\hat{z}) \tag{14}$$

Then, the total remission crossing the dimension of the fiber facet is:

$$R_{remission}^{semi}(\mu_s') = T_{norm} \int_0^{2\pi} d\phi \int_0^{r_{fib}} \left| \vec{J}_{semi}^{z}(\vec{r}_d) \right| \rho \cdot d\rho$$

$$= \frac{1}{2} T_{norm} \left(\exp(-\mu_{eff} z_a) - \frac{z_a}{\sqrt{r_{fib}^2 + z_a^2}} \exp\left(-\mu_{eff}\sqrt{r_{fib}^2 + z_a^2}\right) \right) \tag{15}$$

$$+ \frac{1}{2} T_{norm} \left(\exp(-\mu_{eff}(z_a + 2z_b)) - \frac{z_a + 2z_b}{\sqrt{r_{fib}^2 + (z_a + 2z_b)^2}} \exp\left(-\mu_{eff}\sqrt{r_{fib}^2 + (z_a + 2z_b)^2}\right) \right)$$

Note that setting r_{fib} to infinity in Equation (15) arrives at the total diffuse reflectance from a semi-infinite boundary, which was previously derived in [39] as Equation (20), scaled by T_{norm}, as is shown in the following equation:

$$R_{remission}^{total}(\mu_s') = \frac{1}{2} T_{norm} \cdot \left(\exp(-\mu_{eff} z_a) + \exp\left[-\mu_{eff}(z_a + 2z_b)\right] \right) \tag{16}$$

By expanding the exponential functions in Equation (15) up to the first order term in their respective Taylor series, the absorption dependence is removed to give the following RoR that is associated with the use of a straight-polished fiber in a semi-infinite domain of tissue medium:

$$R_{remission}^{semi}(\mu_s') = \frac{1}{2}(1 - R_{norm}) \cdot \left(1 - \frac{z_a}{\sqrt{r_{fib}^2 + z_a^2}} \right) + \frac{1}{2} \cdot \left(1 - \frac{z_a + 2z_b}{\sqrt{r_{fib}^2 + (z_a + 2z_b)^2}} \right) \tag{17}$$

2.3. Ratio-of-Remission Associated with Steady-State Probing in an Infinite Tissue Geometry Using an Angle-Polished Fiber

We consider the case of interstitial SfRS tissue probing using a fiber with the tip polished at an angle β_{fib}, as conceptually illustrated in Figure 4A. The single-fiber dual-point treatment to the photon trajectory, as is shown in Figure 2B, needs to be modified to that shown in Figure 4B. The symbols introduced in Section 2.1 are used here whenever applicable. Additional symbols/entities in association with the angled fiber facet are given in the following section.

Figure 4. (**A**) Schematic of an idealized geometry for placing a fiber with a diameter of d_{fib} and an angle-polished tip within a turbid medium. The same fiber is used for launching light into and collecting light from the medium. A dual-point configuration approximates the light leaving and returning to the fiber. (**B**) The light that is directionally-launched into the medium along the fiber axis within the fiber refracts to an off-axis direction in the medium. As a result, the equivalent isotropic point source is located at an off-axis position of $\vec{r}_{real}(z_a \sin \beta_{real}, \pi, z_a \cos \beta_{real})$, where $\beta_{real} = \sin^{-1}\left[\left(n_{fiber}/n_{tiss}\right)\sin\beta_{fib}\right]$. The distance between the equivalent point source $\vec{r}_{real}$ and a detector point $\vec{r}_d(\rho, \varphi, 0)$ is l_{real}.
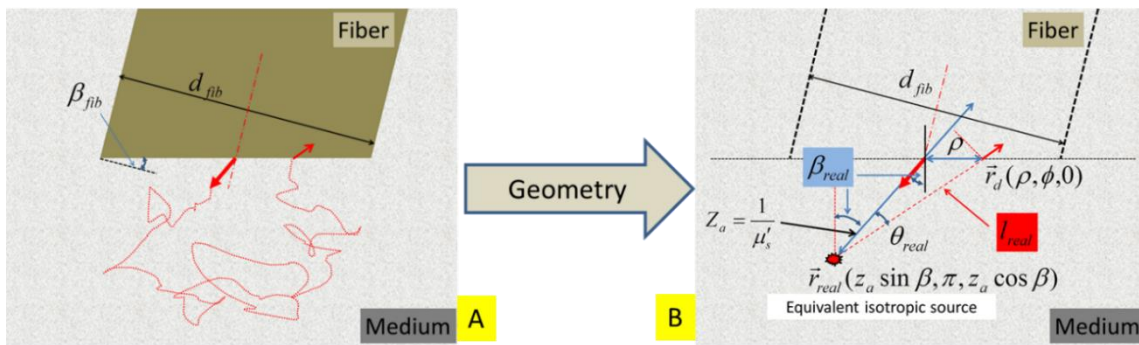
- The on-axis light leaves the fiber facet at an angle of $\beta_{real} = \sin^{-1}\left[\left(n_{fiber}/n_{tiss}\right)\sin\beta_{fib}\right]$. The equivalent isotropic point source is located at $\vec{r}_{real}(z_a \sin\beta_{real}, \pi, z_a \cos\beta_{real})$.

- The distance between the equivalent isotropic point source $\vec{r}_{real}$ and the detector point $\vec{r}_d(\rho, \varphi, 0)$ is

$$l_{real} = \left|\vec{r}_{real} - \vec{r}_d\right| = \sqrt{\rho^2 + z_a^2 + 2\rho\, z_a \sin\beta_{real} \cos\varphi}.$$

The steady-state remission crossing the fiber facet is found by following the approaches of Section 2.1 and after some algebraic derivations to be:

$$^{ang}R_{remission}^{\inf}(\mu_s') = \frac{1}{2}T_{norm}$$

$$\cdot\left(\exp(-\mu_{eff}z_a) - \frac{z_a}{\sqrt{r_{fib}^2 + z_a^2 + 2r_{fib}z_a \sin\beta_{real}}}\exp(-\mu_{eff}\sqrt{r_{fib}^2 + z_a^2 + 2r_{fib}z_a \sin\beta_{real}})\right) \quad (18)$$

As the angle of the fiber polishing β_{fib} approaches zero, the RoR represented by Equation (18) expectedly reaches the one in Equation (10) that corresponds to the RoR of a straight-polished fiber. By expanding the exponential functions of Equation (17) up to the first order term in their respective Taylor series, the absorption dependence is removed to give the following RoR that is associated with the use of an angle-polished fiber in an infinite domain of tissue medium:
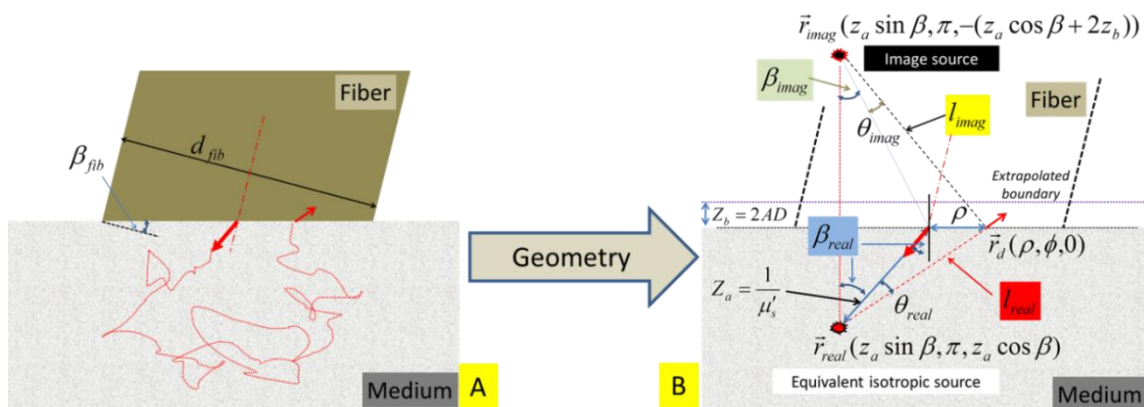
$$^{ang}R_{remission}^{\inf}(\mu_s') = \frac{1}{2}T_{norm}\cdot\left(1 - \frac{z_a}{\sqrt{r_{fib}^2 + z_a^2 + 2r_{fib}z_a \sin\beta_{real}}}\right) \quad (19)$$

2.4. Ratio-of-Remission Associated with Steady-State Probing in a Semi-Infinite Tissue Geometry Using an Angle-Polished Fiber

We consider the case of surface SfRS tissue probing using a fiber with the tip polished at an angle β_{fib} as conceptually illustrated in Figure 5A. The single-fiber dual-point treatment to the photon trajectory in a semi-infinite tissue medium as is shown in Figure 3B needs to be modified to that shown in Figure 5B. The symbols introduced in Section 2.2 are used here whenever applicable. Additional symbols/entities in association with the angled fiber facet are given in the following section.

- The equivalent isotropic point source is located at $\vec{r}_{real}(z_a \sin\beta_{real}, \pi, z_a \cos\beta_{real})$. The image of the isotropic point source with respect to the extrapolated boundary is located at $\vec{r}_{imag}(z_a \sin\beta_{real}, \pi, -(z_a \cos\beta_{real} + 2z_b))$.

- The distance between the "real" point source $\vec{r}_{real}$ and $\vec{r}_d(\rho, \varphi, 0)$ is $l_{real} = |\vec{r}_{real} - \vec{r}_d| = \sqrt{\rho^2 + z_a^2 + 2\rho z_a \sin\beta_{real} \cos\varphi}$. The distance between the image source $\vec{r}_{imag}$ and the detector point $\vec{r}_d(\rho, \varphi, 0)$ is $l_{imag} = |\vec{r}_{imag} - \vec{r}_d| = \sqrt{\rho^2 + z_{imag}^2 + 2\rho z_a \sin\beta_{real} \cos\varphi}$, where $z_{imag} = \sqrt{z_a^2 + 2z_a(2z_b)\cos\beta_{real} + (2z_b)^2}$.

Figure 5. (**A**) Schematic of an idealized geometry for placing a fiber with a diameter of d_{fib} and an angle-polished tip at the surface of a turbid medium. The same fiber is used for launching light into and collecting light from the medium. A dual-point configuration approximates the light leaving and returning to the fiber. (**B**) The light that is directionally-launched into the medium along the fiber axis within the fiber refracts to the off-axis direction in the medium. As a result, the equivalent isotropic source is located at $\vec{r}_{real}(z_a \sin\beta_{real}, \pi, z_a \cos\beta_{real})$. The distance between the equivalent source $\vec{r}_{real}$ and a detector point $\vec{r}_d(\rho, \phi, 0)$ is l_{real}. An "extrapolated" boundary is located at z_b, away from the physical boundary of the medium. The image of the source $\vec{r}_{real}$ w.r.t the "extrapolated" boundary is located at $\vec{r}_{imag}(z_a \sin\beta_{real}, \pi, -(z_a \cos\beta_{real} + 2z_b))$. The distance between the image source $\vec{r}_{imag}$ and the detector point $\vec{r}_d$ is l_{imag}.

The steady-state remission crossing the fiber facet is found to be:

$$^{ang}R_{remission}^{semi}(\mu_s') = \frac{1}{2}T_{norm} \cdot \left(\exp(-\mu_{eff} z_a) - \frac{z_a \exp(-\mu_{eff}\sqrt{r_{fib}^2 + z_a^2 + 2r_{fib}z_a \sin\beta_{real}})}{\sqrt{r_{fib}^2 + z_a^2 + 2r_{fib}z_a \sin\beta_{real}}} \right)$$

$$+\frac{1}{2}T_{norm} \cdot \left(\exp[-\mu_{eff} z_{imag}] - \frac{z_{imag} \exp(-\mu_{eff}\sqrt{r_{fib}^2 + z_{imag}^2 + 2r_{fib}z_{imag} \sin\beta_{imag}})}{\sqrt{r_{fib}^2 + z_{imag}^2 + 2r_{fib}z_{imag} \sin\beta_{imag}}} \right) \quad (20)$$

As the angle of the fiber polishing β_{fib} approaches zero, the RoR represented by Equation (20) for the semi-infinite domain of medium geometry expectedly reaches the one in Equation (15) that corresponds to the RoR of a straight-polished fiber in the same domain. By expanding the exponential functions in Equation (18) up to the first order term in their respective Taylor series, the absorption dependence is removed to give the following RoR that is associated with the use of an angle-polished fiber in a semi-infinite domain of tissue medium:

$$^{ang}R_{remission}^{semi}(\mu_s') = \frac{1}{2}T_{norm} \cdot \left(1 - \frac{z_a}{\sqrt{r_{fib}^2 + z_a^2 + 2r_{fib}z_a \sin\beta_{real}}} \right) + \frac{1}{2}T_{norm} \cdot \left(1 - \frac{z_{imag}}{\sqrt{r_{fib}^2 + z_{imag}^2 + 2r_{fib}z_a \sin\beta_{real}}} \right) \quad (21)$$

3. Numerical Evaluation

By replacing r_{fib} with $d_{fib}/2$ and z_a with $1/\mu_s'$ in the set of Equations (11), (17), (19), and (21), the RoR becomes a function of the dimensionless reduced scattering coefficient $\mu_s'd$, as represented, respectively, in the following for the four cases of probing the tissue with a single fiber:

- The fiber with a straight-polished tip is inserted into the medium to form an infinite domain.

$$R_{remission}^{inf}(\mu_s') = \frac{1}{2}T_{norm} \cdot \left(1 - \frac{2}{\sqrt{4 + (\mu_s'd_{fib})^2}} \right) \quad (22)$$

- The fiber with an angle-polished tip is inserted into the medium to form an infinite domain.

$$^{ang}R_{remission}^{inf}(\mu_s') = \frac{1}{2}T_{norm} \cdot \left(1 - \frac{2}{\sqrt{4 + (\mu_s'd_{fib})^2 + 4(\mu_s'd_{fib})\sin\beta_{real}}} \right) \quad (23)$$

- The fiber with a straight-polished tip is placed in contact with the surface of the medium to form a semi-infinite domain.

$$R_{remission}^{semi}(\mu_s') = \frac{1}{2}T_{norm} \cdot \left(1 - \frac{2}{\sqrt{4 + (\mu_s'd_{fib})^2}} \right) + \frac{1}{2}T_{norm} \cdot \left(1 - \frac{2\left(1 + \frac{4}{3}A\right)}{\sqrt{4\left(1 + \frac{4}{3}A\right)^2 + (\mu_s'd_{fib})^2}} \right) \quad (24)$$

- The fiber with an angle-polished tip is placed in contact with the surface of the medium to form a semi-infinite domain.

$$
{}^{ang}R_{remission}^{semi}(\mu_s') = \frac{1}{2}T_{norm} \cdot \left(1 - \frac{2}{\sqrt{4 + \left(\mu_s'd_{fib}\right)^2 + 4\left(\mu_s'd_{fib}\right)\sin\beta_{real}}} \right)
$$

$$
+ \frac{1}{2}T_{norm} \cdot \left(1 - \frac{2\sqrt{1 + \frac{8}{3}A\cos\beta_{real} + \left(\frac{4A}{3}\right)^2}}{\sqrt{4\left(1 + \frac{8}{3}A\cos\beta_{real} + \left(\frac{4A}{3}\right)^2\right) + \left(\mu_s'd_{fib}\right)^2 + 4\left(\mu_s'd_{fib}\right)\sin\beta_{real}}} \right) \tag{25}
$$

The four cases of analytically-derived RoRs as represented by the set of Equation (19) are evaluated in Figure 6 in comparison to the semi-empirical model of the RoR of Equation (2) over a range of $\mu_s'd_{fib} = \left(10^{-2} \; 10^3\right)$. The parameters for the semi-empirical RoR are chosen as p1 = 6.82, p2 = 0.969, p3 = 1.55, corresponding to those fitted for an HG scattering phase function with g = 0.8 [22]. Fitted parameters corresponding to the HG scattering phase function with other values of g (0.5, 0.7, 0.9) and a modified HG scattering phase function of g = 0.9 are tested. The chosen set of parameters associated with the HG phase function of g = 0.8 leads to the closest patterns between estimation by the empirical equation and estimation by the one specific equation that corresponds to surface probing of the medium using angle-polished fiber (*i.e.*, 25). The red solid line pointed by two arrows corresponds to the "previous semi-empirical" model developed based upon MC studies and experimental measurements from a scattering medium, as specified by Equation (2). The two other solid lines correspond to using a straight-polished fiber in either in-medium probing or surface-probing configurations. The dashed line corresponds to using a 15° angle-polished fiber in an in-medium probing configuration, and the dotted line a surface-probing configuration.

Figure 6. (**A**) Comparisons of analytically-derived ratios-of-remission (RoRs) corresponding to surface-probing or interstitial-probing using a straight- or angle-polished fiber probe, against semi-empirical RoR corresponding to an Henyey–Greenstein (HG) scattering phase function with $g = 0.8$. (**B**) The zoomed-up view of the plots enclosed by the dashed rectangle, as shown in (**A**). The red solid line with two arrows pointing at it corresponds to the "previous semi-empirical" model developed based on MC studies and experimental measurements from a scattering medium. The two other solid lines correspond to using a straight-polished fiber in either in-medium probing or surface-probing configurations. The dashed line corresponds to using a 15 ° angle-polished fiber in in-medium probing configuration, and the dotted line is the surface-probing configuration. The values corresponding to in-medium probing and surface-probing with the fiber of the same tip geometry merge at smaller values of the dimensionless reduced scattering coefficient. The values correspond to a straight-polished fiber and a 15 ° angle-polished fiber in the same condition of fiber placement with the medium converging at higher values of the dimensionless reduced scattering coefficient.
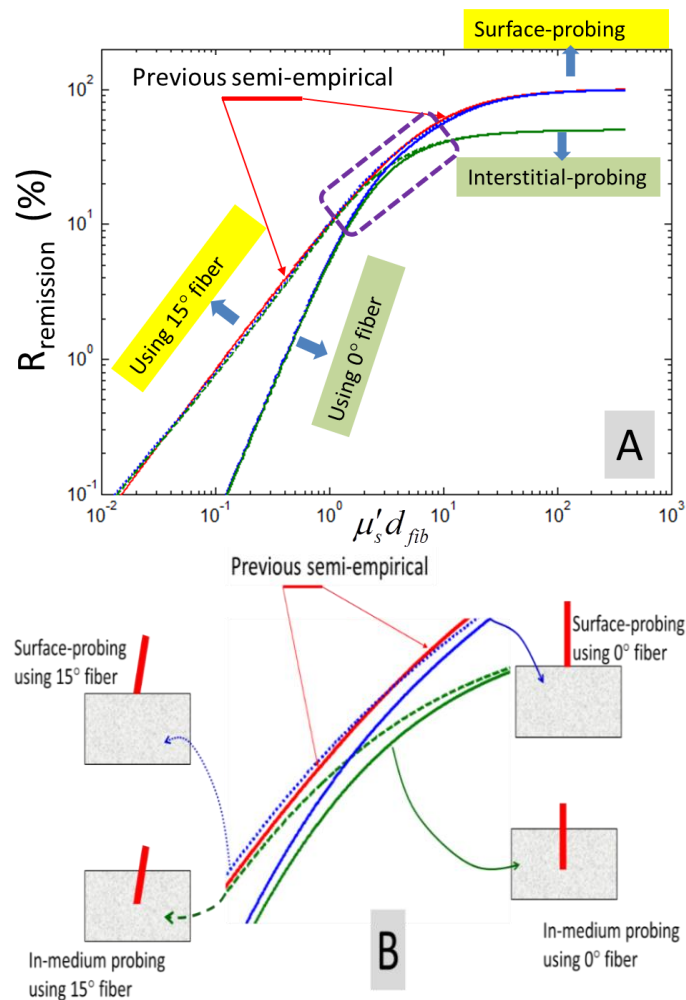
4. Discussion

Several observations can be made from Figure 6, wherein the plot corresponding to the semi-empirical RoR is marked as the solid red line with the two long line-arrows point at it. Firstly, all of the four analytically-derived RoRs show a pattern of monotonic increase *versus* $\mu'_s d_{fib}$ until approximately $\mu'_s d_{fib} > 10$, when approaching an asymptotic limit for high dimensionless, reduced scattering values. Secondly, the surface-probing RoR and interstitial-probing RoR are indistinguishable (at the scale shown) at relatively low dimensionless, reduced scattering values of $\mu'_s d_{fib} < 1$, but differ significantly at high dimensionless, reduced scattering values of $\mu'_s d_{fib} > 10$. At high dimensionless, reduced scattering values, the surface-probing RoR can be as high as twice f the interstitial-probing RoR. The existence of the medium boundary in the surface-probing configuration will cause some photons reaching the boundary to be back-reflected into the medium, adding to the total number of scattering occurring within the medium domain in the vicinity of the probing fiber. The net effect is the essential increase of the number of photons to be scattered into the probing-fiber in surface-probing configuration when comparing to in-medium probing configuration for otherwise identical medium optical properties. Thirdly, the RoR using angle-polished fiber and RoR using straight-polished fiber are indistinguishable (at the scale shown) at high dimensionless, reduced scattering values of $\mu'_s d_{fib} > 10$, but differ significantly at relatively low dimensionless, reduced scattering values of $\mu'_s d_{fib} < 1$. At low dimensionless, reduced scattering values, the RoR using angle-polished fiber can be significantly higher than the RoR using straight-polished fiber. The increased remission associated with using 15 °angle-polished fiber compared to using straight-polished fiber has been suggested to relate to the increased fiber face, as the 15 ° angle-polished fiber has an elliptical cross-section that is about 3% larger than the circular cross-section [22]. We note that as the angle-polished fiber pulls the effective isotropic source closer in depth to the fiber face, the remission obtained by an angle-polished fiber will increase beyond the increase rendered by the bigger fiber face of an elliptical cross-section compared to a circular cross-section of a straight-fiber. Lastly, the analytically-derived RoR corresponding to surface-probing using a 15 ° angle-polished fiber nearly coincides with the semi-empirical RoR corresponding to an HG scattering phase function with $g = 0.8$.

The observation of the agreement between analytical RoR of surface-probing using a 15 ° angle-polished fiber and semi-empirical RoR corresponding to an HG scattering phase function with g = 0.8 is particularly interesting. It is noted that the experimental reports in [21] that validated the empirical RoR were performed at a semi-infinite surface-probing geometry that was in accordance with the geometry of the MC [42]. It is therefore not surprising that it is the RoR derived from surface-probing, not interstitial-probing, medium geometry that shall agree with the semi-empirical results over the range of $\mu'_s d_{fib} > 10$.

Given the agreements between the analytically-derived RoR, with the semi-empirical one notwithstanding, the current analytical treatment is based on isotropic scattering, thereby being incapable of modeling the effect of anisotropic scattering phase function on the remission of photons, particularly in the position near the point-of-entry, as is the case of SfRS. Vitkin *et al.* [43] recently introduced a method to accurately model photon diffusion near the point-of-entry in anisotropically scattering media. Their approach decomposes the diffuse reflectance associated with a semi-infinite

medium-boundary to one part resulting from diffusion approximation and a new part derived for correcting the anisotropic phase function. The phase function-dependent term of the photon fluence rate at a position of $\vec{r}_d(\rho,\phi,0)$ can be derived from [43] as:

$$R_{phase}^{z_a}(\rho) = \mu_s \left[p\left(-\frac{z_a}{\sqrt{\rho^2 + z_a^2}} \right) - \frac{1-g}{4\pi} \right] \exp\left[-\mu_s'(z_a + \sqrt{\rho^2 + z_a^2}) \right] \frac{z_a}{\left(\sqrt{\rho^2 + z_a^2} \right)^3} \qquad (26)$$

where *p* is the actual phase function. It is straightforward to anticipate that incorporating Equation (20) into the analytical approach presented in this work to account for the anisotropic portion of the scattering may result in an analytically-originated formulation of the RoR that responds to the difference in the scattering phase function and anisotropy factor. It is, however, noteworthy to argue that Equation (20) was derived in association with a semi-infinite medium geometry in [43]. It is therefore speculated that a term like Equation (2) that accounts for the anisotropic scattering would have the boundary effect built-in. Once such a boundary-effect term is identified, the contribution to the remission in different SfRS configurations by anisotropic scattering can be isolated according to the analytical procedures demonstrated in this work to possibly reach a set of closed-form solutions. On the other hand, the analytical procedures explored in this work in the condition of isotropic medium scattering are extendable to SfRS in time-of-flight measurements and the fluorescence domain, which may be reported in future publications.

5. Conclusions

In conclusion, this work has presented an isotropic-scattering-based analytical treatment to the ratio-of-remission (RoR) factor that quantifies the ratio of photons remitting from the medium and crossing the fiber face over the total number of photons launched into the medium in steady-state SfRS measurement. This analytically-originated approach is implemented for two fiber-probing geometries, including in-medium SfRS measurement that applies to liquid medium or interstitial probing of biological tissue and surface-based SfRS measurement that applies to solid medium or contact-probing of biological tissue. This analytically originated approach is also conducted for SfRS using straight-polished or angle-polished fiber. It is found that the analytically-computed surface-probing SfRS using a $15°$ angle-polished fiber over the range of $\mu_s' d_{fib} = (10^{-2} \ 10^3)$ agrees with the previously reported MC and experimental studies from a (semi-infinite) medium that has a Henyey–Greenstein scattering phase function with an anisotropy factor of 0.8.

Acknowledgments

Author Contributions

Daqing Piao conceived and developed the analytical works, conducted the numerical implementations, and wrote the manuscript. Joel W. Slaton, in addition to reviewing the manuscript for submission, contributed to the initiation of this study through scientific discussions, specifically regarding the applicability of the investigated spectroscopy technology in urinary bladder regime where accurate modeling of the difference in probing geometry is particularly important to quantitation for tissue diagnosis or photodynamic response monitoring.

Conflicts of Interest

The authors declare no conflict of interest.

References

1. Amelink, A.; Sterenborg, H.J.C.M. Measurement of the local optical properties of turbid media by differential path-length spectroscopy. *Appl. Opt.* **2004**, *43*, 3048–3054.
2. Amelink, A.; Sterenborg, H.J.C.M.; Bard, M.P.; Burgers, S.A. *In vivo* measurement of the local optical properties of tissue by use of differential path-length spectroscopy. *Opt. Lett.* **2004**, *29*, 1087–1089.
3. Moffitt, T.P.; Prahl, S.A. Sized-fiber reflectometry for measuring local optical properties. *IEEE J. Sel. Top. Quantum Electron.* **2001**, *7*, 952–958.
4. Canpolat, M.; Akyuz, M.; Gokhan, G.A.; Gurer, E.I.; Tuncer, R. Intra-operative brain tumor detection usingelastic light single-scattering spectroscopy: A feasibility study. *J. Biomed. Opt.* **2009**, *14*, 054021.
5. Hoy, C.L.; Gamm, U.A.; Sterenborg, H.J.C.M.; Robinson, D.J.; Amelink, A. Use of a coherent fiber bundle for multi-diameter single fiber reflectance spectroscopy. *Biomed. Opt. Express* **2012**, *3*, 2452–2464.
6. Van Leeuwen-van Zaane, F.; Gamm, U.A.; van Driel, P.B.A.A.; Snoeks, T.J.A.; de Bruijn, H.S.; van der Ploeg-van den Heuvel, A.; Mol, I.M.; Löwik, C.W.G.M.; Sterenborg, H.J.C.M.; Amelink, A.; *et al*. *In vivo* quantification of the scattering properties of tissue using multi-diameter single fiber reflectance spectroscopy. *Biomed. Opt. Express* **2013**, *4*, 696–708.
7. Kanick, S.C.; van der Leest, C.; Aerts, J.G.; Hoogsteden, H.C.; Kascakova, S.; Sterenborg, H.J.C.M. Amelink, A. Integration of single-fiber reflectance spectroscopy into ultrasound-guided endoscopic lung cancerstaging of mediastinal lymph nodes. *J. Biomed. Opt.* **2010**, *15*, 017004.
8. Kanick, S.C.; van der Leest, C.; Djamin, R.S.; Janssens, A.M.; Hoogsteden, H.C.; Sterenborg, A. Amelink, H.J.C.M.; Aerts, J.G. Characterization of mediastinal lymph node physiology *in vivo* by optical spectroscopy during endoscopic ultrasound-guided fine needle aspiration. *J. Thorac. Oncol.* **2010**, *5*, 981–987.
9. Piao, D.; McKeirnan, K.L.; Jiang, Y.; Breshears, M.A.; Bartels, K.E. A low-cost needle-based single-fiber spectroscopy method to probe scattering changes associated with mineralization in canine intervertebral disc. *Photonics Lasers Med.* **2012**, *1*, 103–115.

10. Piao, D.; McKeirnan, K.L.; Sultana, N.; Breshears, M.A.; Zhang, A.; Bartels, K.E. Per-cutaneous single-fiber reflectance spectroscopy of canine intervertebral disc: Is there a potential for *in situ* probing of mineral degeneration? *Lasers Surg. Med.* **2014**, *46*, 508–519.

11. Amelink, A.; Kok, D.J.; Sterenborf, H.J.; Scheepe, I.R. *In vivo* measurement of bladder wall oxygen saturation using optical spectroscopy. *J. Biophotonics* **2011**, *4*, 715–720.

12. Pogue, B.W.; Burke, G. Fiber-optic bundle design for quantitative fluorescence measurement from tissue. *Appl. Opt.* **1998**, *37*, 7429–7436.

13. Pfefer, T.J.; Schomacker, K.T.; Ediger, M.N.; Nishioka, N.S. Light propagation in tissue during fluorescence spectroscopy with single-fiber probes. *J. Opt. Soc. Am. B* **2001**, *7*, 1077–1012.

14. Diamond, K.R.; Patterson, M.S.; Farrell, T.J. Quantification of fluorophore concentration in tissuesimulating media by fluorescence measurements with a single optical fiber. *Appl. Opt.* **2003**, *42*, 2436–2442.

15. Stepp, H.; Beck, T.; Beyer, W.; Pfaller, C.; Schuppler, M.; Sroka, R.; Baumgartner, R. Measurement of fluorophore concentration in turbid media by a single optical fiber. *Med. Laser Appl.* **2007**, *22*, 23–34.

16. Canpolat, M.; Mourant, J.R. Particle size analysis of turbid media with a single optical fiber in contact withthe medium to deliver and detect white light. *Appl. Opt.* **2001**, *40*, 3792–3799.

17. Amelink, A.; Bard, M.P.; Burgers, S.A.; Sterenborg, H.J.C.M. Single-scattering spectroscopy for the endoscopic analysis of particle size in superficial layers of turbid media. *Appl. Opt.* **2003**, *42*, 4095–4101.

18. Moffitt, T.P.; Prahl, S.A. The specular reflection problem with a single fiber for emission and collection. In *SPIE Saratov Fall Meeting 2002: Optical Technologies in Biophysics and Medicine IV*; Publisher: Saratov, Russia, 2003.

19. Bargo, P.R.; Prahl, S.A.; Jacques, S.L. Collection efficiency of a single optical fiber in turbid media. *Appl. Opt.* **2003**, *42*, 3187–3197.

20. Kanick, S.C.; Sterenborg, H.J.C.M.; Amelink, A. Empirical model of the photon path length for a single fiber reflectance spectroscopy device. *Opt. Express* **2009**, *17*, 860–871.

21. Kanick, S.C.; Robinson, D.J.; Sterenborg, H.J.C.M.; Amelink, A. Monte Carlo analysis of single fiber reflectance spectroscopy: Photon path length and sampling depth. *Phys. Med. Biol.* **2009**, *54*, 6991–7008.

22. Kanick, S.C.; Gamm, U.A.; Schouten, M.; Sterenborg, H.J.C.M.; Robinson, D.J.; Amelink, A. Measurement of the reduced scattering coefficient of turbid media using single fiber reflectance spectroscopy: Fiber diameter and phase function dependence. *Biomed. Opt. Express* **2011**, *2*, 1687–1702.

23. Gamm, U.A.; Kanick, S.C.; Sterenborg, H.J.C.M.; Robinson, D.J.; Amelink, A. Measurement of tissue scattering properties using multi-diameter single fiber reflectance spectroscopy: *In silico* sensitivity analysis. *Biomed. Opt. Express* **2011**, *2*, 3150–3166.

24. Kanick, S.C.; Robinson, D.J.; Sterenborg, H.J.; Arjen Amelink, C.M. Method to quantitate absorption coefficients from single fiber reflectance spectra without knowledge of the scattering properties. *Opt. Lett.* **2011**, *36*, 2791–2793.

25. Kanick, S.C.; Gamm, U.A.; Sterenborg, H.J.C.M.; Robinson, D.J.; Amelink, A. Method to quantitatively estimate wavelength-dependent scattering properties from multidiameter single fiber reflectance spectra measured in a turbid medium. *Opt. Lett.* **2011**, *36*, 2997–2999.

26. Gamm, U.A.; Kanick, S.C.; Sterenborg, H.J.C.M.; Robinson, D.J.; Amelink, A. Quantification of the reduced scattering coefficient and phase-function-dependent parameter γ of turbid media using multidiameter single fiber reflectance spectroscopy: Experimental validation. *Opt. Lett.* **2012**, *37*, 1838–1840.

27. Mourant, J.R.; Boyer, J.; Hielscher, A.H.; Bigio, I.J. Influence of the scattering phase function on light transport measurements in turbid media performed with small source-detector separations. *Opt. Lett.* **1996**, *21*, 546–548.

28. Kienle, A.; Forster, F.K.; Hibst, R. Influence of the phase function on determination of the optical properties of biological tissue by spatially resolved reflectance. *Opt. Lett.* **2001**, *26*, 1571–1573.

29. Wax, A.; Backman, V. *Biomedical Applications of Light Scattering*; McGraw-Hill: New York, USA, 2010.

30. Yoo, K.M.; Liu, F.; Alfano, R.R. When does the diffusion approximation fail to describe photon transport in random media. *Phys. Rev. Lett.* **1990**, *64*, 2647–2650.

31. Blanco, S.; Fournier, R. Short-path statistics and the diffusion approximation. *Phys. Rev. Lett.* **2006**, *97*, 230604.

32. Lee, C.; Whelan, W.M.; Vitkin, I.A. Information content of point radiance measurements in turbid media: Implications for interstitial optical property quantification. *Appl. Opt.* **2009**, *45*, 2101–2114.

33. Reif, R.; A'Amar, O.; Bigio, I.J. Analytical model of light reflectance for extraction of the optical properties in small volumes of turbid media. *Appl. Opt.* **2007**, *46*, 7317–7328.

34. Hull, E.L.; Foster, T.H. Steady-state reflectance spectroscopy in the P3 approximation. *J. Opt. Soc. Am. A* **2001**, *18*, 584–599.

35. Gomes, A.J.; Backman, V. Analytical light reflectance models for overlapping illumination and collection area geometries. *Appl. Opt.* **2012**, *51*, 8013–8021.

36. Snabre, P.; Arhaliass, A. Anisotropic scattering of light in random media: Incoherent backscattered spotlight. *Appl. Opt.* **1998**, *37*, 4017–4026.

37. Johns, M.; Giller, C.; German, D.; Liu, H. Determination of reduced scattering coefficient of biological tissue from a needle-like probe. *Opt. Express* **2005**, *13*, 4828–4842.

38. Haskell, R.C.; Svaasand, L.O.; Tsay, T.; Feng, T.; McAdams, M.S.; Tromberg, B.J. Boundary conditions for the diffusion equation in radiative transfer. *J. Opt. Soc. Am. A* **1994**, *11*, 2727–2741.

39. Farrell, T.J.; Patterson, M.S.; Wilson, B. A diffusion theory model of spatially resolved, steady-state diffuse reflectance for the noninvasive determination of tissue optical properties *in vivo*. *Med. Phys.* **1992**, *19*, 879–888.

40. Contini, D.; Martelli, F.; Zaccanti, G. Photon migration through a turbid slab described by a model based on diffusion approximation. *Theory Appl. Opt.* **1997**, *36*, 4587–4599.

41. Groenhuis, R.A.J.; Ferwerda, H.A.; Ten Bosch, J.J. Scattering and absorption of turbid materials determined from reflection measurements. *Theory Appl. Opt.* **1983**, *22*, 2456–2462.

42. Wang, L.; Jacques, S.L.; Zheng, L. MCML–Monte Carlo modeling of light transport in multi-layered tissues. *Comput. Methods Progr. Biomed.* **1995**, *47*, 131–146.

43. Vitkin, E.; Turzhitsky, V.; Qiu, L.; Guo, L.; Itzkan, I.; Hanlon, E.B.; Perelman, L.T. Photon diffusion near the point-of-entry in anisotropically scattering turbid media. *Nat. Commun.* **2011**, *13*, 587.